Analytical and Bioanalytical Chemistry
https://doi.org/10.1007/s00216-026-06468-4

PAPER IN FOREFRONT

Capacitive field-effect biosensors loaded with intact plant virus particles: modelling and experimental data

Melanie Welden[1] · Arshak Poghossian[2] · Christina Wege[3] · Michael J. Schöning[1,4]

Received: 7 January 2026 / Revised: 18 March 2026 / Accepted: 19 March 2026

Abstract

Plant viruses are considered one of the main contributors to crop losses in the agricultural industry and thus induce high economic costs worldwide. The best strategy to slow down the spread of plant virus infections and prevent crop failures is to make an early and reliable diagnosis and provide prompt treatment. Electrolyte-insulator-semiconductor capacitors (EISCAP) represent an attractive transducer architecture for label-free electrostatic detection of virus particles by their intrinsic charge. In this work, a capacitive model of an EISCAP sensor loaded with negatively charged *tobacco mosaic virus* (TMV) particles is presented. In the developed model, the adsorbed TMV particles are assumed as local gates with dimensions in the nano- to sub-micrometer range. The impact of TMV surface coverage on the sensor characteristics of SiO_2-gate EISCAPs was studied theoretically and experimentally. The observed EISCAP signal correlates well with the coverage of loaded TMV particles evaluated from scanning electron microscopy images of the SiO_2-gate surface.

Keywords Capacitive field-effect biosensor · Plant virus particles · *Tobacco mosaic virus* · Capacitive model · Virus coverage · Label-free detection

Introduction

Plant viruses are recognized as one of the main contributors to crop losses in the agricultural industry and thus represent a serious threat to global food security. The economic losses caused by plant viruses are substantial and estimated to be between $30 and $60 billion worldwide annually, with increasing impact due to climate change and international transport of plant materials [1, 2]. Early and reliable diagnosis of plant virus infections as well as prompt treatment before disease symptoms appear is the best strategy to slow down the virus spread and prevent crop failures. Therefore, different methods and specialized tools based on the immunological, nucleic acid, and physicochemical features of viruses have been utilized for viral pathogen identification and diagnosis. Although molecular- and immunoassay-based detection technologies possess high sensitivity/specificity and represent the gold standard for providing reliable and accurate virus diagnostics, these tests are expensive, time-consuming, labor-intensive, and require skilled personnel. Moreover, they can be hardly adapted as first-line virus screening tools for on-site (i.e., in-field) applications [3–5]. Lateral-flow immunological assay (LFA) formats have recently received significant attention for point-of-care rapid virus detection [6]. LFA test strips were reported for several plant viruses, including potato virus x [7], banana bract mosaic virus [8], grapevine leafroll-associated virus [9], tobacco mosaic virus (TMV), tobacco vein banding mosaic virus, and potato virus [10]. Although LFA tests are fast, simple-to-use, and disposable, and represent relatively inexpensive diagnostic tools suitable for on-site or in-field plant virus detection, usually they have lower sensitivity and do not offer quantitative results [11].

Published in the topical collection honoring Günter Gauglitz's lifetime achievements.

✉ Arshak Poghossian
a.poghossian@gmx.de

✉ Michael J. Schöning
schoening@fh-aachen.de

[1] Institute of Nano- and Biotechnologies, Aachen University of Applied Sciences, 52428 Jülich, Germany

[2] MicroNanoBio, 53125 Bonn, Germany

[3] Institute of Biomaterials and Biomolecular Systems, University of Stuttgart, 70569 Stuttgart, Germany

[4] Institute of Biological Information Processing (IBI-3), Forschungszentrum Jülich GmbH, 52425 Jülich, Germany

Published online: 01 April 2026

To our knowledge, on-site-based quantitative plant virus diagnostic tests with sensitive characteristics comparable to those of laboratory diagnostic tools are currently not available. As a consequence, samples have to be collected in the field and are typically sent to qualified laboratories for analysis, which is time-consuming and cost-intensive for farmers, since many crops must be monitored repeatedly throughout the cultivation period [11]. Therefore, there is a strong interest to develop highly sensitive, accurate, rapid, cost-efficient, and portable sensor devices for in-field virus detection/identification in randomly selected plants. This should include minimal sample preparation steps and be capable of producing real-time data about viral infections in order to reduce losses in yield as well as the use of expensive, environmentally damaging chemicals. Pesticides inhibiting the transmission of viruses include insecticides, fungicides, and nematicides, all of which may have adverse effects on the host plant, humans, and the environment [12].

In contrast to highly sophisticated analytical lab tools, easily manageable biosensors could simplify the on-site plant virus diagnostics and assist virus disease management, given that they provide sufficient sensitivity and selectivity. During the last years, various biosensor-based approaches (e.g., quartz crystal microbalance [13], surface plasmon resonance [14], electrochemical impedance spectroscopy [15], capacitance measurements [16], and magnetic frequency mixing technique [11]) were proposed for detecting plant virus particles (see also recent reviews [3–5, 17]). Moreover, it has been reported on modern plant-health monitoring systems, which employ an array of various "wearable", wireless sensors installed on the leaves of live plants and Internet of Things technologies for the transmission of measurement data indicating plant tissue invasion by viruses [18, 19].

Among different label-free sensing technologies proposed for virus detection, biosensors with semiconductor-based field-effect devices (BioFEDs) open up new possibilities: BioFEDs are not only able to identify viral antigens or nucleic acids by their intrinsic molecular charge, but also to directly electrostatically detect the adsorption/binding of charged viruses on the gate surface without the use of any label molecules [20–25]. Furthermore, BioFEDs are small in size, have a fast response time, enable real-time and multiplexed measurements, possess robustness, and are compatible with chip fabrication technologies (see, e.g., recent reviews [22, 26–28]). In the past, various types of BioFEDs were successfully implemented for the detection of diverse dangerous human and animal virus particles, such as subtypes of influenza A (H1N1 [29–31], H3N2 [30], H5N1 [31], H5N2 [32]), adenovirus [29], rotavirus [33], human immunodeficiency virus [34], Ebola [35], SARS-CoV-2 [36], etc. As indicated in [21], BioFEDs are able for ultrasensitive, label-free detection of animal and human virus particles.

On the other hand, there are only a few publications related to the detection of plant virus particles with BioFEDs. For example, plum pox virus particles were detected with extended-gate organic field-effect transistors with a lower limit of detection of 180 pg/mL [37]. Our group has, for the first time, studied the possibility of label-free electrical detection of TMV (*tobacco mosaic virus*) particles using electrolyte-insulator-semiconductor capacitors (EISCAP)—the simplest field-effect device—which is a biochemically sensitive capacitor [38, 39]. In contrast to conventional transistor-type devices, EISCAP sensors have a simple layout, which makes them easy and cost-effective in fabrication. It has been observed that the EISCAP signal is influenced by the amount of adsorbed TMV particles on the EISCAP surface [38, 39]. However, this effect has not yet been modeled, evaluated, or discussed in detail.

In this work, we present the capacitive model of an EISCAP biosensor loaded with the charged, nanorod-shaped TMV particles. The influence of surface coverage of TMV on the EISCAP response (i.e., capacitance–voltage (*C*–*V*) characteristics) has been studied. TMV was chosen as a model plant virus, because:

a) it is one of the most infectious plant pathogens. It has been reported that TMVs infect more than 400 species of 36 botanical families, inducing mosaic-like patterns on the leaves and reduced growth of many hosts (e.g., pepper, tomato, aubergine, tobacco, etc.) [12], while they are non-pathogenic and non-hazardous for animals or humans [40]. In spite of a deep understanding of the TMV structure and its transmission routes, TMV causes considerable financial losses of more than 100 million dollars worldwide each year [2];
b) our group has many years of expertise with enzyme-based biosensors (EISCAPs) decorated with TMV particles utilized as enzyme nanocarriers [41–45].

Capacitive model of EISCAP covered with TMV particles

The schematic structure of an EISCAP sensor chip loaded with TMV particles is illustrated in Fig. 1a. It comprises a Si substrate, which is separated from the solution by a gate-insulator film (in this work, SiO_2), and a backside metal (Al) contact layer. Native TMV is composed of about 2130 identical coat proteins helically assembled around the single-stranded viral ribonucleic acid (see, e.g., [46]). The TMV particle has a rigid nanotube-like structure of 300 nm length complete particles, with an outer diameter of 18 nm and an inner diameter of 4 nm (nucleoprotein tube: aspect ratio ≈ 17). The isoelectric point of TMV is at pH 3.5 [47]; TMV particles are negatively charged in solutions with pH > 3.5.

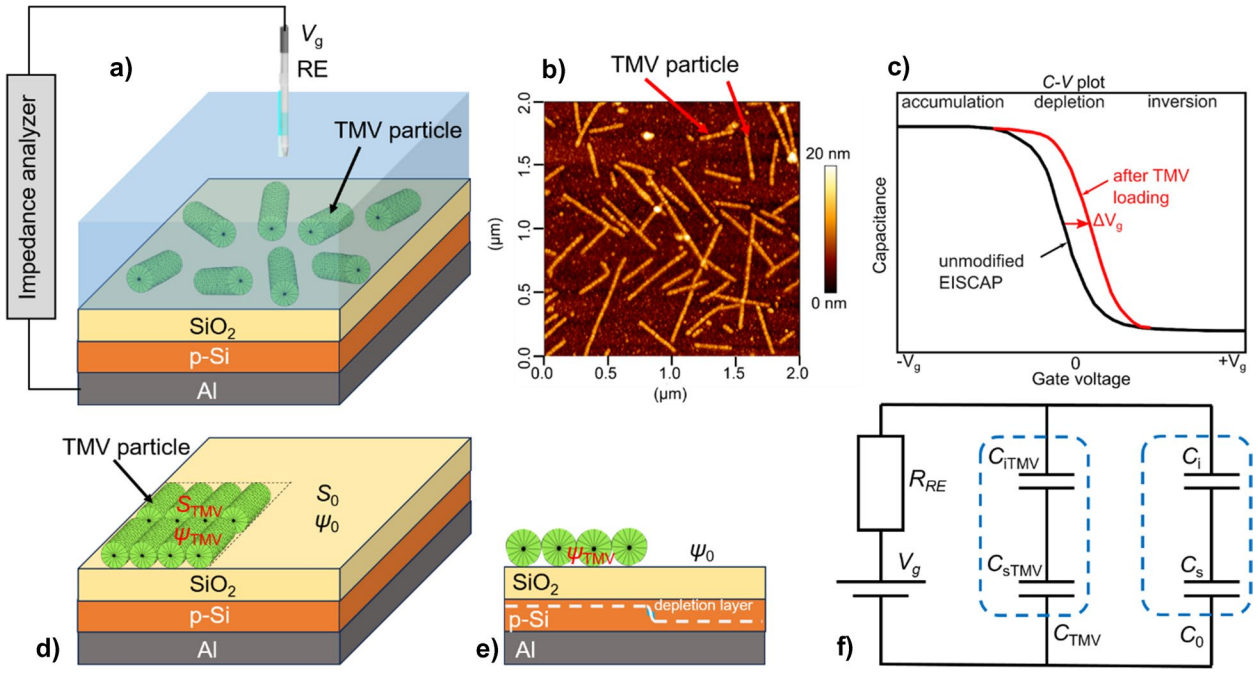

Fig. 1 **a** EISCAP structure loaded with TMV particles (schematically); **b** AFM image of the SiO_2-gate surface loaded with TMV particles collected in tapping mode (BioMAT Workstation, JPK Instruments, Berlin, Germany); **c** characteristic high-frequency *C–V* plot for a p-type EISCAP biosensor before and after TMV adsorption with accumulation, depletion and inversion region, respectively; **d** EISCAP surface with TMV-covered and TMV-free regions (schematically); **e** depletion layer profile in p-Si underneath regions covered with TMV and TMV-free regions (schematically); and **f** simplified electrical equivalent circuit of the TMV-covered EISCAP. RE, reference electrode; V_g, gate voltage; ΔV_g, shift of the $C-V$ plot along the voltage axis; S_{TMV} and S_0, surface areas of TMV-covered and TMV-free regions, respectively; ψ_{TMV} and ψ_0, gate-surface potentials in TMV-covered and TMV-free regions, respectively; R_{RE}, resistance of the RE; C_{iTMV}, C_{sTMV}, and C_{TMV}, gate-insulator, depletion-layer, and overall capacitances in the TMV-covered region, respectively; C_i, C_s, and C_0, gate-insulator, depletion-layer, and overall capacitances in the TMV-free region, respectively

Our previous experiments demonstrate that because of inter-particle repulsion as well as electrostatic and other interactions between TMV particles and the gate insulator surface, negatively charged TMV particles usually do not form an ordered and densely packed layer. This behavior is evident, for example, on SiO_2 surfaces [39], which themselves carry a negative charge over a broad pH range (reported points of zero charge for SiO_2 are approximately pH 2.66–2.8 [48]).

The exemplary AFM image of TMVs on the SiO_2-gate EISCAP surface (see Fig. 1b) shows randomly distributed TMV particles with a large inter-particle spacing. Similar effects were observed, for instance, for TMV adsorbed on bare [49] or oxidized [50] Si substrates as well as on Ta_2O_5-gate EISCAPs [41], and may be explained by the immobility of TMV particles on the substrate surface [49]: adsorbed particles become "frozen" upon deposition, resulting in predominantly random orientation.

In addition to pH- [51, 52] and ion-sensitive [53] features, EISCAPs are known as transducer structures for designing various enzyme-based logic gates [54, 55] and as charge-sensitive devices, capable of label-free, electrical detection of adsorption/binding of various charged biomolecules (see, e.g., [56–59]) and (bio)nanoparticles (including TMV particles) on their gate surface [38, 39, 48, 60, 61]. Because of the presence of a space-charge (depletion) region nearby the semiconductor/gate-insulator interface, EISCAPs possess a variable total capacitance, which depends, among others, on the impressed gate voltage and the charge of adsorbed/bound species, such as charged TMV. Our proposed approach is based on the idea that adsorbed TMV particles represent nanometer-sized local gates, which will locally affect the space-charge distribution in the Si; in a first approximation, we neglect a possible overlapping of the local space-charge regions in the semiconductor (by, e.g., the fringing effect [62]).

For instance, in case of p-type Si, negatively charged TMV particles onto the gate-insulator surface will decrease the width of the depletion layer and increase the space-charge capacitance in the Si within regions underneath surface areas covered with TMV. As a consequence, the total capacitance of the EISCAP will increase as well, resulting in a shift of the capacitance–voltage (*C–V*) characteristics (one of the most convenient modes of electrochemical characterization of EISCAPs [26, 63]) in the direction of more positive (or less negative) gate voltages (Fig. 1c, red curve).

The amplitude of this potential shift (ΔV_g) reflects potential changes at the gate surface induced by the adsorption/binding of charged TMV particles.

Thus, owing to the operating principle of an EISCAP sensor, its response will depend on the fraction of the surface area covered with TMV particles (i.e., on the TMV surface coverage). Hence, the EISCAP loaded with charged TMV can be divided into two regions (Fig. 1d):

a) a TMV-covered region with a surface area S_{TMV}, gate-surface potential ψ_{TMV} and TMV coverage $\theta = S_{\mathrm{TMV}}/S$, where S is the complete EISCAP surface area in contact with the electrolyte;
b) a TMV-free region with a surface area $S_0 = (1-\theta)S$ and a gate-surface potential ψ_0.

For the EISCAP application as a biosensor to detect diverse biomolecules and (bio-)nanoparticles by their intrinsic charge, the most useful range of the *C–V* plot is the depletion region (see Fig. 1c). Here, the total EISCAP capacitance is more sensitive to charge or potential changes at/nearby the gate surface. The expected change in profile of the depletion layer in the p-Si underneath the TMV-covered region is schematically depicted in Fig. 1e. To evaluate the impact of TMV coverage on the *C–V* curve, we derived the expression for the equivalent capacitance of the TMV-covered EISCAP in the depletion state.

The simplified electrical equivalent circuit of the TMV-covered EISCAP is illustrated in Fig. 1f. As discussed in [26, 64, 65], for a typical layer structure of the EISCAP and measuring conditions used, the resistances, such as the Al/Si backside contact, the bulk Si, the electrolyte solution and the double-layer capacitance (electrolyte/gate-insulator interface), can be neglected. Hence, the electrical equivalent circuit of a TMV-loaded EISCAP biosensor can be simplified as a parallel connection of two capacitances, C_0 and C_{TMV} (see Fig. 1f).

The term C_0 is the total capacitance associated with the TMV-free region and composed of the gate-insulator capacitance ($C_{\mathrm{i}} = C_{\mathrm{i0}}S(1-\theta)$) and the depletion-layer capacitance in the Si underneath the TMV-free region ($C_{\mathrm{s}} = C_{\mathrm{s0}}S(1-\theta)$) in series:

$$C_0 = \frac{C_i C_s}{C_i + C_s} = \frac{C_{i0}C_{s0}S(1-\theta)}{C_{i0} + C_{s0}} \tag{1}$$

where $C_{\mathrm{i0}} = \varepsilon_{\mathrm{i}}\varepsilon_0/d_{\mathrm{i}}$ is the capacitance of the gate insulator per unit surface area, ε_{i} and d_{i} are the dielectric constant and thickness of the gate insulator, respectively, ε_0 is the vacuum permittivity, $C_{\mathrm{s0}} = \varepsilon_{\mathrm{s}}\varepsilon_0/w_{\mathrm{s}}$ represents the capacitance of the depletion layer in the Si per unit surface area, and ε_{s} and w_{s} are the dielectric constant of Si and width of the depletion layer, respectively. Analogously, the total capacitance C_{TMV} associated with the TMV-covered region is a series connection of the gate-insulator ($C_{\mathrm{iTMV}} = C_{\mathrm{i0}}S\theta$) and the semiconductor depletion-layer ($C_{\mathrm{sTMV}} = C_{\mathrm{s0TMV}}S\theta$) capacitance (Fig. 1f):

$$C_{TMV} = \frac{C_{iTMV}C_{sTMV}}{C_{iTMV} + C_{sTMV}} = \frac{C_{i0}C_{s0TMV}S\theta}{C_{i0} + C_{s0TMV}} \tag{2}$$

where $C_{\mathrm{s0TMV}} = \varepsilon_{\mathrm{s}}\varepsilon_0/w_{\mathrm{sTMV}}$ and w_{sTMV} represent the capacitance per unit surface area and the width of the depletion layer in the Si (TMV-covered region), respectively.

The equivalent capacitance (C_{eq}) of the whole EISCAP chip can be calculated by combining the total capacitances of the TMV-covered and TMV-free regions in parallel:

$$C_{eq} = C_{TMV} + C_0 = \frac{C_{i0}C_{s0TMV}S\theta}{C_{i0} + C_{s0TMV}} + \frac{C_{i0}C_{s0}S(1-\theta)}{C_{i0} + C_{s0}} \tag{3}$$

To examine the impact of the TMV coverage on the *C–V* plot of the EISCAP, we have to derive the expressions for the depletion-layer capacitances per active surface area in the Si underneath the TMV-covered and TMV-free regions (i.e., C_{s0TMV} and C_{s0}). These capacitances can be deduced from the equation for the depletion capacitance of a metal–oxide–semiconductor (MOS) structure (C_{s0MOS}) per unit surface area [65, 66]

$$C_{s0MOS} = \frac{1}{\sqrt{\frac{1}{C_{i0}^2} + \frac{2(V_g - V_{fbMOS})}{qN_A\varepsilon_s\varepsilon_0}} - \frac{1}{C_{i0}}} \tag{4}$$

by replacing the flatband voltage V_{fbMOS} of the MOS capacitor

$$V_{fbMOS} = \frac{W_M - W_S}{q} - \frac{Q_i + Q_{ss}}{C_{i0}} \tag{5}$$

by the flatband voltage (V_{fb}) of the EISCAP [65, 67]:

$$V_{fb} = E_{ref} - \psi + \chi_{sol} - \frac{W_S}{q} - \frac{Q_i + Q_{ss}}{C_{i0}} \tag{6}$$

In Eqs. (4)–(6), V_{g} is the gate voltage, N_{A} describes the density of ionized acceptors, q is the elementary charge, W_{M} and W_{S} are the metal and the silicon electron work functions, respectively, Q_{i} and Q_{ss} are the charges located in the oxide and the surface and interface states (for simplicity, in further description it is assumed that Q_{i} and Q_{ss} are zero), E_{ref} is the potential of the reference electrode, and χ_{sol} is the surface-dipole potential of the solution. The term ψ denotes the gate-surface potential: In this work, we hypothesize that $\psi = \psi_0$ for the TMV-free region, $\psi = \psi_{\mathrm{TMV}} = \psi_0 + \Delta\psi_{\mathrm{TMV}}$ for the TMV-covered region, and $\Delta\psi_{\mathrm{TMV}}$ is the gate-surface potential change induced due to adsorbed charged TMV particles. The potential (ψ_0) at the

interface electrolyte/pH-sensitive gate-insulator (such as SiO_2 used in this study) is given by [68, 69]:

$$\psi_0 = 2.3\frac{kT}{q}\alpha\left(pH_{PZC} - pH\right) \tag{7}$$

where k is the Boltzmann constant, T is the temperature of the solution (in K), pH_{pzc} represents the pH value at the point of zero charge, and α is the ratio of the real pH sensitivity of the gate insulator to the ideal Nernstian sensitivity (59.16 mV/pH at room temperature).

Alternatively, the capacitances C_{s0TMV} and C_{s0} can be derived from Eq. (4) by replacing V_g with the effective gate voltage (V_{g-eff}), which is given by [68, 70]:

$$V_{g-eff} = V_G - E_{ref} + \psi - \chi_{sol} + W_m/q \tag{8}$$

resulting in the following equations for C_{s0TMV} and C_{s0}:

$$C_{s0TMV} = \frac{1}{\left[1/C_{i0}^2 + 2\left(V_g - E_{ref} - \chi_{sol} + \psi_0 + \triangle\psi_{TMV} + W_s/q\right)/q\varepsilon_s\varepsilon_0 N_a\right]^{1/2} - 1/C_{i0}}, \tag{9}$$

$$C_{s0} = \frac{1}{\left[1/C_{i0}^2 + 2\left(V_g - E_{ref} - \chi_{sol} + \psi_0 + W_s/q\right)/q\varepsilon_s\varepsilon_0 N_a\right]^{1/2} - 1/C_{i0}}. \tag{10}$$

By substituting Eqs. (9) and (10) into expression (3), we obtain the following equation for the equivalent capacitance (C_{eq}) of the TMV-loaded EISCAP in the depletion region:

$$C_{eq} = S\theta\left\{\frac{1}{\left[1/C_{i0}^2 + 2\left(V_g - E_{ref} - \chi_{sol} + \psi_0 + \Delta\psi_{TMV} + W_s/q\right)/q\varepsilon_s\varepsilon_0 N_a\right]^{1/2}} - \frac{1}{\left[1/C_{i0}^2 + 2\left(V_g - E_{ref} - \chi_{sol} + \psi_0 + W_s/q\right)/q\varepsilon_s\varepsilon_0 N_a\right]^{1/2}}\right\} + \frac{S}{\left[1/C_{i0}^2 + 2\left(V_g - E_{ref} - \chi_{sol} + \psi_0 + W_s/q\right)/q\varepsilon_s\varepsilon_0 N_a\right]^{1/2}} \tag{11}$$

Equation (11) includes two TMV-related terms, namely, the TMV coverage (θ) and the gate-surface potential change caused via the adsorbed charged TMV particles ($\Delta\psi_{TMV}$). In the depletion region, the equivalent capacitance of the TMV-loaded EISCAP linearly depends on the TMV surface coverage. A simplified relationship between $\Delta\psi_{TMV}$ and the effective TMV charge (Q_{TMV}) is given by:

$$\Delta\psi_{TMV} = N_{TMV}Q_{TMV}/C_{dl} \tag{12}$$

where N_{TMV} is the theoretical maximum surface density of densely packed TMV nanotubes with an outer diameter of 18 nm and a length of 300 nm ($N_{TMV} \sim 2\times10^{12}$ TMV/cm^2) and C_{dl} is the electrical double-layer capacitance per unit surface area in the TMV-covered region.

There are large discrepancies about the net surface charge of TMV particles reported in the literature [47, 71, 72], which ranges from 90 to 1800 elementary charges per virus particle dependent on the solution's pH and ionic strength. The partial screening of the TMV charge by mobile counter ions in the analyte affects the EISCAP response, which is mainly defined by the Debye length (inversely proportional to ionic strength) and by the distance between the EISCAP surface and the effective TMV charge [73, 74]. Since TMV particles exhibit nanotubular structures, their charge is not confined directly to the EISCAP surface, but distributed over a certain distance away from the EISCAP surface. With increasing electrolyte concentration, the effectivity of electrostatic coupling between the charged TMV particles and the EISCAP surface as well as the fraction of the effective TMV charge, which will still remain inside the Debye length (i.e., detectable by the EISCAP biosensor) will decrease. Simultaneously, the double-layer capacitance (C_{dl}) will increase. As a result, the gate-surface potential changes ($\Delta\psi_{TMV}$, see Eq. (12)) caused via adsorbed charged TMV particles will decrease. Hence, generally, to achieve a large biosensor signal while detecting charged TMV particles with EISCAPs, low ionic-strength electrolyte solutions are preferred that have been experimentally evidenced in [39]. If the C–V characterization of TMV-loaded EISCAPs is carried out in solutions with a constant pH and ionic strength (as in this study), $\Delta\psi_{TMV}$ can be considered approximately constant.

We have simulated the equivalent capacitance of the TMV-loaded EISCAP and C–V plots in the depletion

region as a function of TMV coverage utilizing Eq. (11). In the model simulations, all terms in Eq. (11), except V_g and θ, were considered constant. The following parameters were used for the simulations: $\varepsilon_0 = 8.854 \times 10^{-12}$ F/m, $\varepsilon_i = 3.9$ (SiO_2), $d_i = 30$ nm, $\varepsilon_s = 11.7$ (Si), $S = 50.24$ mm^2, $N_A = 6.2 \times 10^{15}$ cm^{-3} (corresponding to resistivity of a Si wafer of 2.54 Ω•cm), $q = 1.6 \times 10^{-19}$ C, a group of TMV-independent potentials $V_{i\text{-}p} = E_{ref} + \chi_{sol} - W_s/q = 0$, $\psi_0 = -40$ mV, $\theta = 0$, 0.2, 0.4, 0.6, 0.8, and 1. For the gate-surface potential change in the region covered with adsorbed charged TMV particles, we selected a value of $\Delta\psi_{TMV} = -30$ mV. This value is related to the results of zeta-potential (−30.7 mV in pH 7 solution) measurements of the biotinylated TMV particles presented in [39] and was used as a working assumption for the simulations.

Simulated *C–V* plots of a p-type EISCAP (in depletion region) without and with negatively charged TMV particles of various surface coverages are depicted in Fig. 2a. As expected, at a constant V_g, loading with negatively charged TMV particles on the EISCAP surface results in an increase in the equivalent capacitance and will shift the *C–V* curve of the bare EISCAP (without TMV particles) towards more positive gate voltages. With increasing TMV coverage, the amount of the voltage shifting is increased. The equivalent-capacitance changes (at $V_g = 90$ mV) and voltage shifts (at $C_{eq} = 38$ nF) as a function of TMV coverage, calculated from the *C–V* curves in Fig. 2a, are illustrated in Fig. 2b.

It should be noted that in our simplified model, the TMV charge (Q_{TMV}) and therefore the gate-surface potential change ($\Delta\psi_{TMV}$) caused via the adsorbed charged TMV particles are considered constant (at a fixed ionic strength). However, the nanotubular structure of TMV particles causes that the TMV charge is not confined directly to the sensor surface, instead being distributed through some distance (depending on Debye length) away from the EISCAP surface. On the other hand, at higher surface coverages, the TMV–TMV interactions and proximity effects may become non-negligible. All these factors may result in a more complicated distribution of both the surface potential and the profile of the depletion layer in the p-Si underneath the TMV-covered region. Therefore, to find out the impact of the amplitude of surface potential changes (or TMV charge, see Eq. (12)) on both the equivalent-capacitance changes and gate-voltage shifts, we additionally simulated

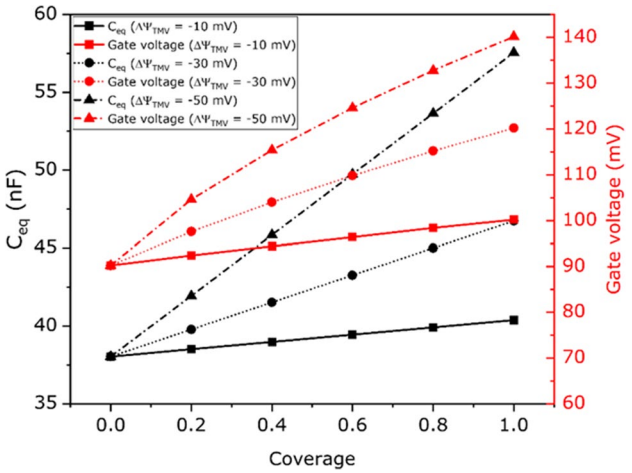

Fig. 3 Equivalent-capacitance changes and voltage shifts as a function of TMV coverage, evaluated from the *C–V* curves simulated at various $\Delta\psi_{TMV}$ values of −10 mV, −30 mV, and −50 mV

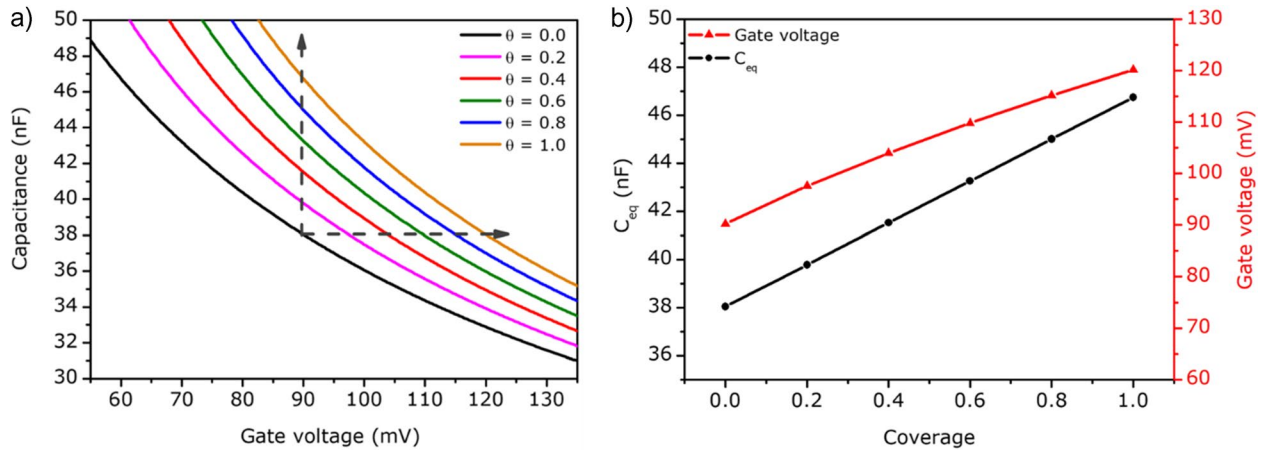

Fig. 2 **a** Simulated *C–V* curves of an unmodified p-type EISCAP (black line) and an EISCAP loaded with negatively charged TMV particles with different coverages θ; **b** equivalent-capacitance changes (at a constant $V_g = 90$ mV) and voltage shifts (at a constant $C_{eq} = 38$ nF) as a function of TMV coverage, calculated from the *C–V* curves

the *C–V* curves at different $\Delta\psi_{TMV}$ values. As an example, Fig. 3 depicts the equivalent-capacitance changes and voltage shifts as a function of TMV coverage, evaluated from the *C–V* curves simulated at various $\Delta\psi_{TMV}$ values of −10 mV, −30 mV, and −50 mV. The analysis of Eq. (11) as well as the evaluation results in Fig. 3 reveal that at a constant TMV coverage, the raise of the $\Delta\psi_{TMV}$ (or Q_{TMV}) increases the slope of both the equivalent-capacitance changes and gate-voltage shifts, resulting in an enhanced EISCAP sensitivity to TMV.

Experimental

Fabrication of EISCAP chips

EISCAP chips composed of a SiO_2/p-Si/Al layer structure were fabricated from a ca. 380 µm thick p-Si wafer (Siegert Wafer, Aachen, Germany) wit <100> orientation and a specific resistivity of 1–5 Ω•cm. A 30 nm SiO_2 gate-insulator film was prepared onto the p-Si by thermal dry oxidation at 1000 °C for about 30 min. In the next step, the SiO_2 layer on the backside of the p-Si was etched with 5% hydrofluoric acid, followed by electron-beam deposition of a ~300 nm thick Al layer to provide the rear-side electrical contact to the p-Si. Finally, the wafer was annealed in N_2 atmosphere at 400 °C for 10 min and then diced into 10 mm × 10 mm single chips. Before application, the EISCAP chips were cleaned in an ultrasonic bath successively with acetone, isopropanol, ethanol and deionized water (each 5 min). Afterwards, the cleaned EISCAPs chips were mounted into a home-made measurement cell and sealed by an O-ring (Viton), protecting the side walls and the Al backside contact from the solution. The remaining front-side surface area of the SiO_2 in contact with the solution, accessible for TMV loading, is determined via the O-ring's inner diameter of (~8 mm) with about 50.24 mm^2. Before electrochemical characterization of EISCAPs, the SiO_2-gate surface was conditioned in Titrisol buffer solution of pH 7 (Merck, Germany) for at least 12 h. This procedure typically allows to achieve a more stable EISCAP signal.

Loading of TMV particles

In this study, we used a genetically modified TMV variant with a cysteine residue exposed on each coat protein. The TMV particles were isolated from infected tobacco plants, purified and biotinylated (for details, see [42, 75]). The stock solution of TMV particles with a concentration of 5 µg/µL (corresponding to 125 nM TMV) in 10 mM sodium–potassium-phosphate buffer (SPP) prepared from 10 mM NaH_2PO_4 (Merck, Darmstadt, Germany) and 10 mM K_2HPO_4 (Carl Roth, Karlsruhe, Germany), pH 7, was stored at 4 °C.

To obtain different surface coverages, the TMV particles were loaded from differently concentrated TMV solutions. Therefore, TMV solutions with different concentrations of 20, 100, and 200 ng/µL (corresponding to 0.5, 2.5, and 5 nM) were diluted from the TMV stock solution with 100 mM SPP buffer (pH 7, ionic strength 150 mM). For TMV particle loading, 50 µL of the differently concentrated TMV solutions were drop-coated onto the SiO_2 surface of separate EISCAP chips, installed in the appropriate measurement cells. Incubation took place at room temperature in a humid chamber. Different incubation times have been reported in the literature for loading TMV particles onto various substrates, that is, from 20 min up to 18 h (see, e.g., [38]). For example, the impact of incubation time on the density of TMV particles loaded from a 100 ng/µL TMV solution on a Ta_2O_5-gate EISCAP surface has been discussed in [38]. Increasing incubation time from 1 to 24 h had only a small effect on the surface density of TMV particles (~ 15%). Overall, TMV loading is nearly completed within ~ 1 h incubation time. Therefore, we decided to operate with an incubation time of 1 h. Then, the gate surfaces of the EISCAPs were rinsed with 0.33 mM phosphate-buffered saline (PBS, pH 7) to remove unattached TMV particles. The detection of the adsorbed intact TMV particles was validated by *C–V*-mode measurements. The pH value of all solutions was additionally controlled via a commercial pH-glass electrode (Mettler Toledo, Giessen, Germany). Overall, eight EISCAP sensors with TMV particles loaded from differently concentrated TMV solutions of 20 ng/µL (three EISCAPs), 100 ng/µL (three EISCAPs), and 200 ng/µL (two EISCAPs) were characterized.

Results and discussion

Field-effect detection of TMV particles by their intrinsic charge with EISCAPs operating in the *C – V* mode

The high-frequency *C–V* plots of EISCAPs before (bare sensor) and after loading with different concentrations of intact virus particles were recorded using an impedance analyzer (Zahner Zennium, Zahner Elektrik, Kronach, Germany). The custom-made measurement cell with the installed EISCAP chip together with the Ag/AgCl reference electrode (RE, filled with 3 M KCl, Metrohm, Filderstadt, Germany) was inserted in a Faraday cage to preclude possible impact of electromagnetic fields and ambient light influence on the EISCAP biosensor response. For C–V-mode operation, a

sweeping direct-current gate voltage (between −2 V and 2 V in 0.1 V increments) and a small superimposed alternating-current voltage (0.02 V with a frequency of $f = 120$ Hz) were applied between the RE and the backside Al contact (see Fig. 1a). To reduce the influence of the Debye screening effect and to achieve a high EISCAP signal change induced by the attached TMV particles, the study was performed in a low ionic-strength (5 mM) buffer (0.33 mM PBS, pH 7, at room temperature).

In the presence of a series resistance (R_{RE}) of the RE (other series resistances can be neglected as discussed in "Capacitive model of EISCAP covered with TMV particles"), the relationship between the measured capacitance (C_m) and the equivalent capacitance (C_{eq}) is defined by [76]:

$$C_m = \frac{C_{eq}}{1 + (2\pi f R_{RE} C_{eq})^2} \tag{13}$$

For our experimental conditions, the term $(2\pi f R_{RE} C_{eq})^2 << 1$. Hence, the measured capacitance can be considered approximately equal to the equivalent capacitance, $C_m \approx C_{eq}$.

Figure 4 depicts exemplary C–V plots of EISCAP sensors in the depletion region recorded before and after loading with different concentrations of TMV particles (Fig. 4a–c). As expected, the adsorption of charged virus particles on the EISCAP surface resulted in a TMV concentration-dependent shift of the original (without TMV particles) C–V plot along the voltage axis. The direction of these shifts corresponds to more negatively charged gate surfaces (see also discussion in "Capacitive model of EISCAP covered with TMV particles") indicating the successful loading of negatively charged TMV particles on the sensor chip. At the same time, the amplitude of the signal shifts gives information about the surface coverage and amount of adsorbed virus particles per EISCAP chip and therefore allows for the establishment of a relationship between the TMV concentration in solution and the TMV coverage. With rising TMV concentration from 20

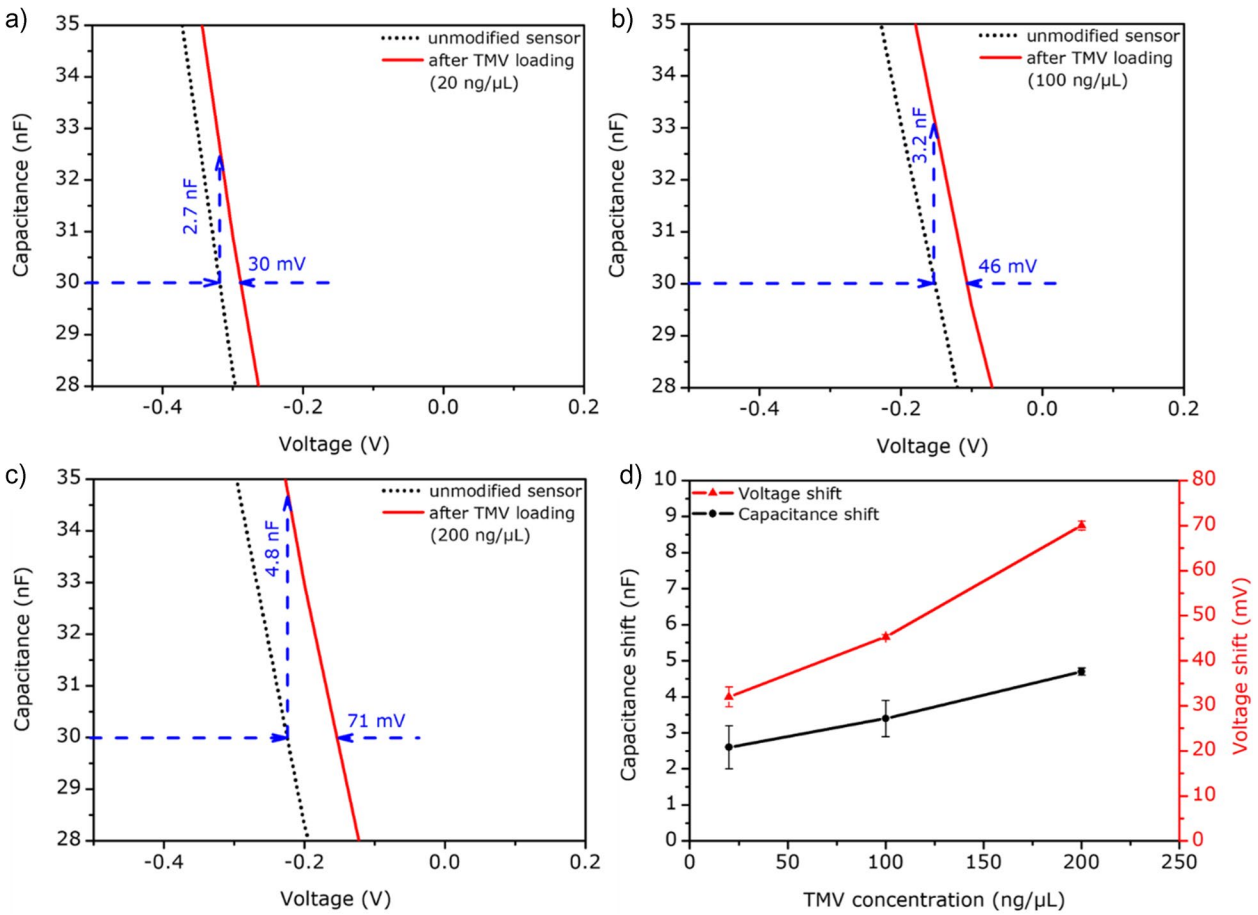

Fig. 4 Exemplary C–V plots of EISCAPs in the depletion region (zoom-in for applied gate voltages between −0.5 and 0.2 V) recorded before and after loading with different concentrations of TMV particles: **a** 20 ng/µL, **b** 100 ng/µL, **c** 200 ng/µL; **d** mean changes in the measured total capacitance (black line) of the TMV-covered EISCAPs in the depletion region and the mean amplitude (red line) of the voltage shifts (at a constant capacitance of 30 nF) as a function of TMV concentration in solution evaluated from the respective C–V plots

to 200 ng/µL, both the measured capacitance change and the shift of the *C–V* plot due to the adsorption of TMV particles increased from 2.7 to 4.8 nF and from 30 to 71 mV, respectively. Remarkably, even the lowest TMV concentration of 20 ng/µL was detectable with the EISCAP biosensor, having a signal of 30 mV.

The mean changes in the measured total capacitance of the TMV-covered EISCAPs in the depletion region (at a constant gate voltage corresponding to a capacitance of 30 nF for the unmodified EISCAP) and the mean amplitude of the voltage shifts (at a constant capacitance of 30 nF), calculated from the respective *C–V* plots, are depicted in Fig. 4d. The mean TMV sensitivity of SiO_2-gate EISCAPs amounted to 35 ± 1.4 mV/dec (or about 2.1 nF/dec) in the TMV concentration range from 20 to 200 ng/µL (0.5–5 nM). The lower detection limit was estimated according to Ref. [77] by the intersection between the calibration curve and the mean background signal plus threefold background standard deviation. The evaluation of the detection limit for TMV particles using the experimental data presented in Fig. 4d reveals that EISCAPs are able to detect TMV particles as low as ~ 1 ng/µL.

Impact of TMV surface coverage on the EISCAP signal

To examine the impact of TMV coverage on the EISCAP signal, SEM images were collected from the active surface area (in contact with solution) of EISCAPs loaded from differently concentrated TMV solutions. Therefore, after *C–V* characterization, the TMV-decorated EISCAPs were demounted from the measurement cell, washed with

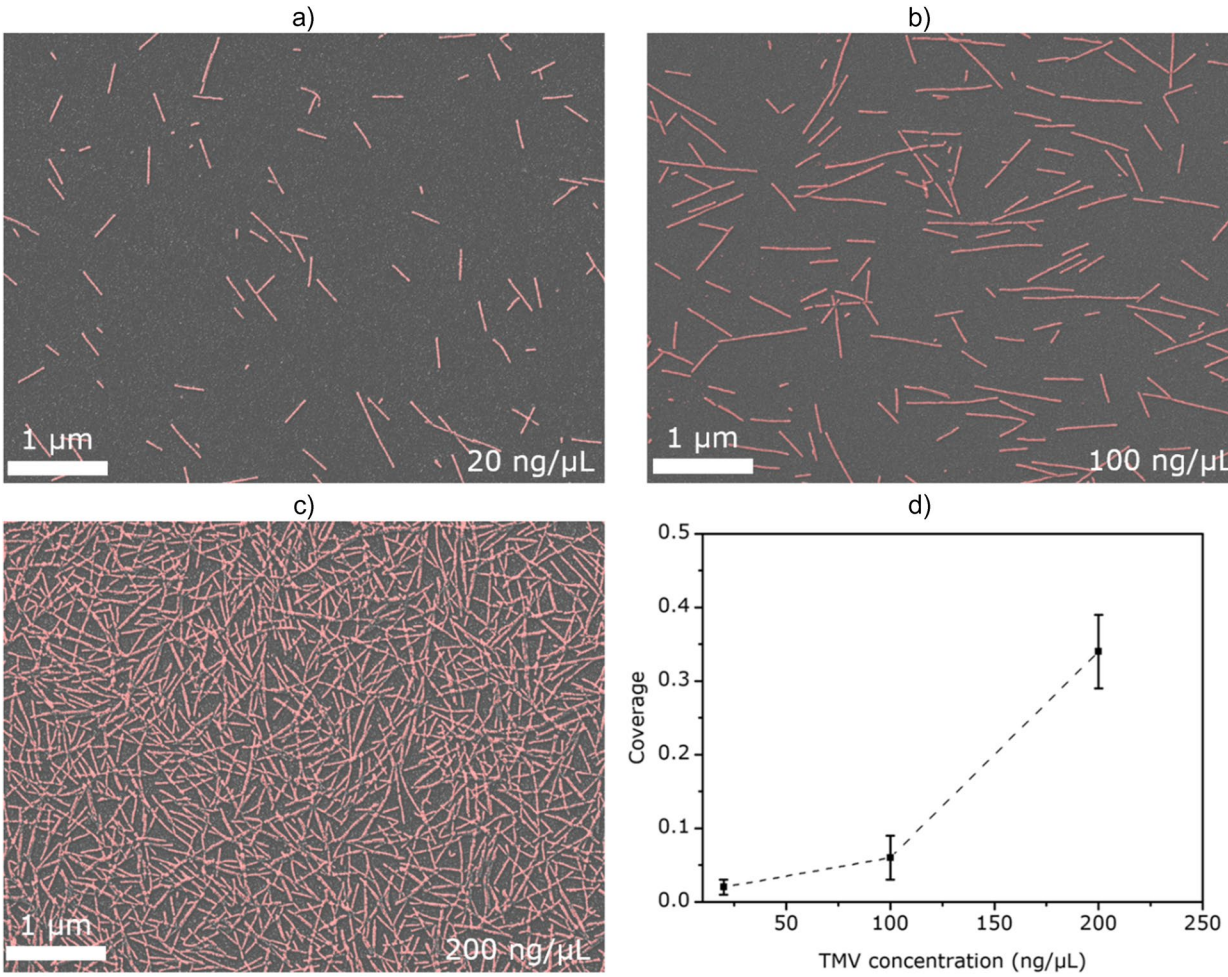

Fig. 5 Exemplary SEM images of EISCAP surfaces loaded with TMV particles from differently concentrated TMV solutions: **a** 20 ng/µL, **b** 100 ng/µL, and **c** 200 ng/µL; **d** mean TMV coverage on the SiO_2-gate EISCAP surfaces evaluated from SEM images (n = 6 representative areas of each EISCAP chip surface) as a function of TMV concentration in solution

deionized water, and prepared for SEM characterization. SEM images were taken from six representative areas of each EISCAP chip surface using a high-resolution Jeol JSM-7800F Schottky field-emission microscope (JEOL GmbH, Freising, Germany).

Figure 5 shows SEM images of EISCAP surfaces with loaded TMV particles from differently concentrated TMV solutions (20 to 200 ng/µL). In the SEM images, randomly oriented, single complete 300 nm long TMV particles, longer particles of more than 600 nm formed by end-to-end aggregation as well as disintegrated shorter TMV fragments or particle intermediates (having lengths from 50 to 200 nm) are clearly visible. In addition, the virus network contained complete and/or incomplete TMVs, which randomly overlapped with each other, thereby forming a partial bilayer or jackstraws configuration rather than a monolayer (see, e.g., SEM image in Fig. 5c). A higher number of adsorbed TMV particles (and therefore, an increased surface coverage) was found with higher TMV concentration in solution. This corresponds to results when loading TMV particles on a gold-covered Si wafer [78] and a Ta_2O_5 surface [38].

To determine the density of TMV particles on the EISCAP surface from SEM images, in our previous experiments, the number of differently sized as well as overlapped virus particles was multiplied by several predetermined correction factors [38, 39, 45]. Then, the evaluated number of TMV particles per EISCAP chip was used to calculate the surface coverage of densely packed TMV nanotubes with an outer diameter of 18 nm and a length of 300 nm. However, such an approach may provoke distinct errors with regard to the real surface coverage of TMV particles and evaluation of the EISCAP signal.

In the present study, we used a proprietary Python-based program to quantify the TMV coverage on the EISCAP surface. The algorithm identifies TMV-covered regions based on image contrast and labels these areas accordingly (displayed as red in the SEM images, Fig. 5). The surface coverage is then calculated from the ratio of the labeled area to the total imaged area. This method allows direct determination of the TMV surface coverage more accurately and without the use of various correction factors for calculating differently sized TMV particles.

Table 1 Correlation between the mean TMV surface coverage (θ) and mean EISCAP signal changes: gate-voltage (ΔV_g) and measured capacitance (ΔC) shifts, respectively

θ	ΔV_g (mV)	ΔC (nF)
0.02 ± 0.01	32 ± 2	2.6 ± 0.6
0.06 ± 0.03	45 ± 0.5	3.4 ± 0.5
0.34 ± 0.05	70 ± 1	4.7 ± 0.1

The mean TMV coverage on the SiO_2-gate EISCAP surfaces evaluated from SEM images (n = 6 representative areas of each EISCAP chip) as a function of TMV concentration in solution is depicted in Fig. 5d. With increasing the TMV concentration in solution from 20 ng/µL to 200 ng/µL, the mean surface coverage increased from $\theta = 0.02 \pm 0.01$ to $\theta = 0.34 \pm 0.05$ (maximum mean TMV coverage achieved in this study).

Table 1 illustrates the correlation between the TMV coverage and the EISCAP signal change, i.e., the gate-voltage and capacitance shift, respectively. As predicted by the capacitive model described in "Capacitive model of EISCAP covered with TMV particles", the higher the TMV coverage, the larger are the recorded *C–V* signal shifts induced by the adsorbed TMV particles. For example, with increasing the TMV coverage from 0.02 to 0.34, the amplitude of mean signal shifts raises from 32 to 70 mV (gate-voltage shift) or 2.6 nF to 4.7 nF (measured capacitance change).

The quantitative comparison of simulated and experimental results seems to be very difficult because Eq. (11) includes some parameters where the values are not exactly known by experimental conditions used in this work (e.g., the doping concentration in Si (N_A), gate-surface potential change caused via the adsorbed charged TMV particles ($\Delta\psi_{TMV}$), effective TMV charge (Q_{TMV}), electrical double-layer capacitance per unit surface area in the TMV-covered region (C_{dl}), and surface-dipole potential of the solution (χ_{sol})).

Conclusions

A capacitive model of an EISCAP sensor loaded with negatively charged TMV particles as a model plant pathogen is presented, in which the adsorbed TMV particles are assumed as local gates in the nanometer size range that locally affect the space-charge distribution and depletion capacitance in the Si. The impact of TMV surface coverage on the *C–V* characteristics of Al-Si-SiO_2 EISCAPs was studied theoretically and experimentally. Different TMV coverages ($\theta = 0.02$, 0.06, and 0.34) on the EISCAP gate surface were achieved by means of TMV loading from differently concentrated TMV solutions of 20, 100, and 200 ng/µL, respectively. The mean surface coverage of TMV particles was evaluated from SEM images for six representative areas of each EISCAP chip surface using a proprietary Python-based program.

Both the simulation and the experimental results reveal that there is a good correlation between the TMV coverage and the EISCAP signal change. While raising the coverage of negatively charged TMV particles, both the measured capacitance changes (at a constant V_g) and the shifts of the original *C–V* curve (at a constant capacitance) towards

more positive (or less negative) gate voltages increased. The EISCAP biosensor can detect TMV particles with concentrations as low as 20 ng/µL, having a mean signal amplitude of 30 mV.

The obtained results demonstrate significant influence of the virus surface coverage on the EISCAP biosensor response, which should be taken into account while developing EISCAP-based quantitative plant virus detectors. In future work, the developed model for the EISCAP sensor loaded with TMV particles will be extended to also consider the impact of overlapping TMV particles and depletion regions as well as the charge-screening and fringing effects on the EISCAP signal. Such a procedure will allow us to gain deeper insight into this novel sensing platform for a label-free electrostatic detection of viruses.

Acknowledgements The authors would like to thank David Rolka, Heiko Iken, and Tobias Karschuck for technical support and Suren Felekyan for simulations.

Author contribution Conceptualization: Melanie Welden, Arshak Poghossian, and Michael J. Schöning. Methodology: Melanie Welden, Arshak Poghossian, Christina Wege, and Michael J. Schöning. Validation: Melanie Welden, Arshak Poghossian, and Michael J. Schöning. Formal analysis: Melanie Welden, Arshak Poghossian, and Michael J. Schöning. Investigation: Melanie Welden and Arshak Poghossian. Writing: Melanie Welden, Arshak Poghossian, Christina Wege, and Michael J. Schöning. Supervision: Arshak Poghossian and Michael J. Schöning.

All authors have read and agreed to the published version of the manuscript.

Funding Open Access funding enabled and organized by Projekt DEAL. This work was funded by the Deutsche Forschungsgemeinschaft (DFG: German Research Foundation) – 446507449.

Data availability Data are available upon request from the authors.

Code availability Code is available upon request from the authors.

Declarations

Conflict of interest The authors declare no competing interests.

References

1. Hilaire J, Tindale S, Jones G, Pingarron-Cardenas G, Bačnik K, Ojo M, et al. Risk perception associated with an emerging agri-food risk in Europe: plant viruses in agriculture. Agriculture & Food Security. 2022;11:21. https://doi.org/10.1186/s40066-022-00366-5.
2. Chen J, Luo X, Chen Y, Wang Y, Peng J, Xing Z. Recent research progress: discovery of anti-plant virus agents based on natural scaffold. Front Chem. 2022;10:926202. https://doi.org/10.3389/fchem.2022.926202.
3. Fang Y, Ramasamy RP. Current and prospective methods for plant disease detection. Biosensors. 2015;5:537–61. https://doi.org/10.3390/bios5030537.
4. Khater M, de la Escosura-Muñiz A, Merkoçi A. Biosensors for plant pathogen detection. Biosens Bioelectron. 2017;93:72–86. https://doi.org/10.1016/j.bios.2016.09.091.
5. Ozer T, Geiss BJ, Henry CS. Review–chemical and biological sensors for viral detection. J Electrochem Soc. 2020;167:037523. https://doi.org/10.1149/2.0232003JES.
6. Ince B, Sezgintürk MK. Lateral flow assays for viruses diagnosis: up-to-date technology and future prospects. Trends Anal Chem. 2022;157:116725. https://doi.org/10.1016/j.trac.2022.116725.
7. Safenkova I, Zherdev A, Dzantiev B. Factors influencing the detection limit of the lateral-flow sandwich immunoassay: a case study with potato virus X. Anal Bioanal Chem. 2012;403:1595–605.
8. Selvarajan R, Selvam KP, Balasubramanian V, Sundaram SS. A rapid and sensitive lateral flow immunoassay (LFIA) test for the on-site detection of banana bract mosaic virus in banana plants. J Virol Methods. 2020;284:113929. https://doi.org/10.1016/j.jviromet.2020.113929.
9. Byzova NA, Vinogradova SV, Porotikova EV, Terekhova UD, Zherdev AV, Dzantiev BB. Lateral flow immunoassay for rapid detection of grapevine leafroll-associated virus. Biosensors. 2018;8:111. https://doi.org/10.3390/bios8040111.
10. Guo Y, Wu W, Zhang X, Ding M, Yu J, Zhang J, et al. Triplex lateral flow immunoassay for rapid diagnosis of tobacco mosaic viruses, tobacco vein banding mosaic virus, and potato virus. Plant Dis. 2022;106:3033–9. https://doi.org/10.1094/PDIS-08-21-1756-RE.
11. Rettcher S, Jungk F, Kühn C, Krause H-J, Nölke G, Commandeur U, et al. Simple and portable magnetic immunoassay for rapid detection and sensitive quantification of plant viruses. Appl Environ Microbiol. 2015;81:3039–48. https://doi.org/10.1128/AEM.03667-14.
12. Trojak-Goluch A. The use of bacteria, actinomycetes and fungi in the bioprotection of solanaceous crops against tobacco mosaic virus (TMV). Agriculture. 2024;14:1220. https://doi.org/10.3390/agriculture14081220.
13. Dickert FL, Hayden O, Bindeus R, Mann KJ, Blaas D, Waigmann E. Bioimprinted QCM sensors for virus detection – screening of plant sap. Anal Bioanal Chem. 2004;378:1929–34. https://doi.org/10.1007/s00216-004-2521-5.
14. Boltovets PM, Snopok BA, Boyko VR, Shevchenko TP, Dyachenko NS, Shirshov YM. Detection of plant viruses using a surface plasmon resonance via complexing with specific antibodies. J Virol Methods. 2004;121:101–6.
15. Ambrico M, Ambrico PF, Minafra A, De Stradis A, Vona D, Cicco SR, et al. Highly sensitive and practical detection of plant

viruses via electrical impedance of droplets on textured silicon-based devices. Sensors. 2016;16:1946. https://doi.org/10.3390/s16111946.
16. Al Ahmad M, Mustafa F, Ali LM, Karakkat JV, Rizvi TA. Label-free capacitance-based identification of viruses. Sci Rep. 2015;5:9809. https://doi.org/10.1038/srep09809.
17. Patel R, Mitra B, Vinchurkar M, Adami A, Patkar R, Giacomozzi F, et al. A review of recent advances in plant-pathogen detection systems. Heliyon. 2022;8:e11855. https://doi.org/10.1016/j.heliyon.2022.e11855.
18. Hossain NI, Tabassum S. A hybrid multifunctional physicochemical sensor suite for continuous monitoring of crop health. Sci Rep. 2023;13:9848. https://doi.org/10.1038/s41598-023-37041-z.
19. Kohzuma K, Miyamoto K. Analysis of plant physiological responses based on leaf color changes through the development and application of a wireless plant sensor. Sens Biosens Res. 2024;46:100688. https://doi.org/10.1016/j.sbsr.2024.100688.
20. de Moraes A, Kubota L. Recent trends in field-effect transistors-based immunosensors. Chemosensors. 2016;4:20. https://doi.org/10.3390/chemosensors4040020.
21. Poghossian A, Jablonski M, Molinnus D, Wege C, Schöning MJ. Field-effect sensors for virus detection: from Ebola to SARS-CoV-2 and plant viral enhancers. Front Plant Sci. 2020;11:598103. https://doi.org/10.3389/fpls.2020.598103.
22. Poghossian A, Schöning MJ. Recent progress in silicon-based biologically sensitive field-effect devices. Curr Opin Electrochem. 2021;29:100811. https://doi.org/10.1016/j.coelec.2021.100811.
23. Li H, Li D, Chen H, Yue X, Fan K, Dong L, et al. Application of silicon nanowire field effect transistor (SiNW-FET) biosensor with high sensitivity. Sensors. 2023;23:6808. https://doi.org/10.3390/s23156808.
24. Zou J, Bai H, Zhang L, Shen Y, Yang C, Zhuang W, et al. Ion-sensitive field effect transistor biosensors for biomarker detection: current progress and challenges. J Mater Chem B. 2024;12:8523–42. https://doi.org/10.1039/D4TB00719K.
25. Zhang Z, Hu J-J, Lin S, Wu J, Xia F, Lou X. Field effect transistor biosensors for healthcare monitoring. Interdiscip Med. 2024;2:e20240032. https://doi.org/10.1002/INMD.20240032.
26. Poghossian A, Schöning MJ. Capacitive field-effect EIS chemical sensors and biosensors: a status report. Sensors. 2020;20:5639. https://doi.org/10.3390/s20195639.
27. Cao S, Sun P, Xiao G, Tang Q, Sun X, Zhao H, et al. ISFET-based sensors for (bio)chemical applications: a review. Electrochem Sci Adv. 2023;3:e2100207. https://doi.org/10.1002/elsa.202100207.
28. Sarcina L, Macchia E, Tricase A, Scandurra C, Imbriano A, Torricelli F, et al. Enzyme based field effect transistor: state-of-the-art and future perspectives. Electrochem Sci Adv. 2023;3:e2100216. https://doi.org/10.1002/elsa.202100216.
29. Patolsky F, Zheng G, Hayden O, Lakadamyali M, Zhuang X, Lieber CM. Electrical detection of single viruses. Proc Natl Acad Sci U S A. 2004;101:14017–22. https://doi.org/10.1073/pnas.0406159101.
30. Shen F, Wang J, Xu Z, Wu Y, Chen Q, Li X, et al. Rapid flu diagnosis using silicon nanowire sensor. Nano Lett. 2012;12:3722–30. https://doi.org/10.1021/nl301516z.
31. Hideshima S, Hayashi H, Hinou H, Nambuya S, Kuroiwa S, Nakanishi T, et al. Glycan-immobilized dual-channel field effect transistor biosensor for the rapid identification of pandemic influenza viral particles. Sci Rep. 2019;9:11616. https://doi.org/10.1038/s41598-019-48076-6.
32. Chiang P-L, Chou T-C, Wu T-H, Li C-C, Liao C-D, Lin J-Y, et al. Nanowire transistor-based ultrasensitive virus detection with reversible surface functionalization. Chem Asian J. 2012;7:2073–9. https://doi.org/10.1002/asia.201200222.
33. Liu F, Kim YH, Cheon DS, Seo TS. Micropatterned reduced graphene oxide based field-effect transistor for real-time virus detection. Sens Actuators B. 2013;186:252–7. https://doi.org/10.1016/j.snb.2013.05.097.
34. Kim JW, Kim S, Jang Y-H, Lim K-I, Lee WH. Attomolar detection of virus by liquid coplanar-gate graphene transistor on plastic. Nanotechnology. 2019;30:345502. https://doi.org/10.1088/1361-6528/ab0f52.
35. Jin X, Zhang H, Li Y-T, Xiao M-M, Zhang Z-L, Pang D-W, et al. A field effect transistor modified with reduced graphene oxide for immunodetection of Ebola virus. Microchim Acta. 2019;186:223. https://doi.org/10.1007/s00604-019-3256-5.
36. Seo G, Lee G, Kim MJ, Baek S-H, Choi M, Ku KB, et al. Rapid detection of COVID-19 causative virus (SARS-CoV-2) in human nasopharyngeal swab specimens using field-effect transistor-based biosensor. ACS Nano. 2020;14:5135–42. https://doi.org/10.1021/acsnano.0c02823.
37. Berto M, Vecchi E, Baiamonte L, Condò C, Sensi M, Di Lauro M, et al. Label free detection of plant viruses with organic transistor biosensors. Sens Actuators B. 2019;281:150–6. https://doi.org/10.1016/j.snb.2018.10.080.
38. Jablonski M, Poghossian A, Severins R, Keusgen M, Wege C, Schöning MJ. Capacitive field-effect biosensor studying adsorption of tobacco mosaic virus particles. Micromachines. 2021;12:57. https://doi.org/10.3390/mi12010057.
39. Jablonski M, Poghossian A, Keusgen M, Wege C, Schöning MJ. Detection of plant virus particles with a capacitive field-effect sensor. Anal Bioanal Chem. 2021;413:5669–78. https://doi.org/10.1007/s00216-021-03448-8.
40. Calo A, Eiben S, Okuda M, Bittner AM. Nanoscale device architectures derived from biological assemblies: the case of tobacco mosaic virus and (apo)ferritin. Jpn J Appl Phys. 2016;55:03DA01. https://doi.org/10.7567/JJAP.55.03DA01.
41. Poghossian A, Jablonski M, Koch C, Bronder TS, Rolka D, Wege C, et al. Field-effect biosensor using virus particles as scaffolds for enzyme immobilization. Biosens Bioelectron. 2018;110:168–74. https://doi.org/10.1016/j.bios.2018.03.036.
42. Koch C, Poghossian A, Schöning MJ, Wege C. Penicillin detection by tobacco mosaic virus-assisted colorimetric biosensors. Nanotheranostics. 2018;2:184–96. https://doi.org/10.7150/ntno.22114.
43. Welden M, Poghossian A, Vahidpour F, Wendlandt T, Keusgen M, Wege C, et al. Towards multi-analyte detection with field-effect capacitors modified with tobacco mosaic virus bioparticles as enzyme nanocarriers. Biosensors. 2022;12:43. https://doi.org/10.3390/bios12010043.
44. Welden M, Severins R, Poghossian A, Wege C, Bongaerts J, Siegert P, et al. Detection of acetoin and diacetyl by a tobacco mosaic virus-assisted field-effect biosensor. Chemosensors. 2022;10:218. https://doi.org/10.3390/chemosensors10060218.
45. Welden M, Poghossian A, Vahidpour F, Wendlandt T, Keusgen M, Wege C, et al. Capacitive field-effect biosensor modified with a stacked bilayer of weak polyelectrolyte and plant virus particles as enzyme nanocarriers. Bioelectrochemistry. 2023;151:108397. https://doi.org/10.1016/j.bioelechem.2023.108397.
46. Fan XZ, Pomerantseva E, Gnerlich M, Brown A, Gerasopoulos K, McCarthy M, et al. Tobacco mosaic virus: a biological building block for micro/nano/bio systems. J Vac Sci Technol A. 2013;31:050815. https://doi.org/10.1116/1.4816584.
47. Alonso JM, Gorzny MŁ, Bittner AM. The physics of tobacco mosaic virus and virus-based devices in biotechnology. Trends Biotechnol. 2013;31:530–8. https://doi.org/10.1016/j.tibtech.2013.05.013.
48. Poghossian A, Karschuck T, Wagner P, Schöning MJ. Field-effect capacitors decorated with ligand-stabilized gold nanoparticles: modeling and experiments. Biosensors. 2022;12:334. https://doi.org/10.3390/bios12050334.

49. Yang L, Wang S, Fukuto M, Checco A, Niu Z, Wang Q. Structure and interaction in 2D assemblies of tobacco mosaic viruses. Soft Matter. 2009;5:4951–61. https://doi.org/10.1039/B911894B.
50. Lee B, Lo C-T, Thiyagarajan P, Winans RE, Li X, Niu Z, et al. Effect of interfacial interaction on the cross-sectional morphology of tobacco mosaic virus using GISAXS. Langmuir. 2007;23:11157–63. https://doi.org/10.1021/la7009989.
51. Molinnus D, Iken H, Johnen AL, Richstein B, Hellmich L, Poghossian A, et al. Miniaturized pH-sensitive field-effect capacitors with ultrathin Ta_2O_5 films prepared by atomic layer deposition. Phys Status Solidi A. 2022;219:2100660. https://doi.org/10.1002/pssa.202100660.
52. Karschuck T, Schmidt S, Achtsnicht S, Poghossian A, Wagner P, Schöning MJ. Multiplexing system for automated characterization of a capacitive field-effect sensor array. physica status solidi (a). 2023;220:2300265. https://doi.org/10.1002/pssa.202300265.
53. Cho H, Kim K, Meyyappan M, Baek CK. LaF_3 electrolyte-insulator-semiconductor sensor for detecting fluoride ions. Sens Actuat B. 2019;279:183–8. https://doi.org/10.1016/j.snb.2018.09.094.
54. Poghossian A, Malzahn K, Abouzar MH, Mehndiratta P, Katz E, Schöning MJ. Integration of biomolecular logic gates with field-effect transducers. Electrochim Acta. 2011;56:9661–5. https://doi.org/10.1016/j.electacta.2011.01.102.
55. Moseley F, Halamek J, Kramer F, Poghossian A, Schöning MJ, Katz E. An enzyme-based reversible CNOT logic gate realized in a flow system. Analyst. 2014;139:1839–42. https://doi.org/10.1039/C4AN00133H.
56. Pan TM, Lin TW, Chen CY. Label-free detection of rheumatoid factor using YbY_xO_y electrolyte-insulator-semiconductor devices. Anal Chim Acta. 2015;891:304–11. https://doi.org/10.1016/j.aca.2015.08.014.
57. Hlukhova H, Menger M, Offenhäusser A, Vitusevich S. Highly sensitive aptamer-based method for the detection of cardiac biomolecules on silicon dioxide surfaces. MRS Adv. 2016;3:1535–41. https://doi.org/10.1557/adv.2018.332.
58. Bahri M, Baraket A, Zine N, Ali MB, Bausells J, Errachid A. Capacitance electrochemical biosensor based on silicon nitride transducer for TNF-α cytokine detection in artificial human saliva: Heart failure (HF), Talanta. Talanta. 2020;209:120501. https://doi.org/10.1016/j.talanta.2019.120501.
59. Bronder TS, Jessing MP, Poghossian A, Keusgen M, Schöning MJ. Detection of PCR-amplified tuberculosis DNA fragments with polyelectrolyte-modified field-effect sensors. Anal Chem. 2018;90:7747–53. https://doi.org/10.1021/acs.analchem.8b01807.
60. Poghossian A, Bäcker M, Mayer D, Schöning MJ. Gating capacitive field-effect sensors by the charge of nanoparticle/molecule hybrids. Nanoscale. 2015;7:1023–31. https://doi.org/10.1039/C4NR05987E.
61. Karschuck T, Kaulen C, Poghossian A, Wagner PH, Schöning MJ. Gold nanoparticle-modified capacitive field-effect sensors: studying the surface density of nanoparticles and coupling of charged polyelectrolyte macromolecules. Electrochem Sci Adv. 2021;2:e2100179. https://doi.org/10.1002/elsa.202100179.
62. Yang C-F, Hwu J-G. Role of fringing field on the electrical characteristics of metal-oxide-semiconductor capacitors with co-planar and edge-removed oxides. AIP Adv. 2016;6:125017. https://doi.org/10.1063/1.4971845.
63. Klein M. Characterisation of ion-sensitive layer systems with a c (V) measurement method operating at constant capacitance. Sens Actuators B. 1990;1:354–6. https://doi.org/10.1016/0925-4005(90)80229-S.
64. Fabry P, Laurent-Yvonnou L. The c–v method for characterizing ISFET or EOS devices with ion-sensitive membranes. J Electroanal Chem Interfacial Electrochem. 1990;286:23–40. https://doi.org/10.1016/0022-0728(90)85062-A.
65. Poghossian A, Welden R, Buniatyan VV, Schöning MJ. An array of on-chip integrated, individually addressable capacitive field-effect sensors with control gate: design and modelling. Sensors. 2021;21:6161. https://doi.org/10.3390/s21186161.
66. Sze SM, Ng KK. Physics of Semiconductor Devices. 3rd ed. Hoboken, New Jersey: John Wiley & Sons; 2007.
67. Bergveld P. A critical evaluation of direct electrical protein detection methods. Biosens Bioelectron. 1991;6:55–72. https://doi.org/10.1016/0956-5663(91)85009-L.
68. Georgiou P, Toumazou C. CMOS-based programmable gate ISFET. Electron Lett. 2008;44:1289–91. https://doi.org/10.1049/el:20082268.
69. Pookaiyaudom P, Lidgey FJ, Hayatleh K, Seelanan P, Toumazou C. Chemical current conveyor (CCCII+): system design and verification for buffer index/capacity measurement. Sens Actuators B Chem. 2010;147:228–33. https://doi.org/10.1016/j.snb.2010.03.037.
70. Shepherd L, Toumazou C. Weak inversion ISFETs for ultra-low power biochemical sensing and real-time analysis. Sens Actuators B Chem. 2005;107:468–73. https://doi.org/10.1016/j.snb.2004.11.006.
71. Wadu-Mesthrige K, Pati B, McClain WM, Liu G-Y. Disaggregation of tobacco mosaic virus by bovine serum albumin. Langmuir. 1996;12:3511–5. https://doi.org/10.1021/la9508506.
72. Wang S, Fukuto M, Checco A, Niu Z, Wang Q, Yang L. Role of electrostatic interactions in two-dimensional self-assembly of tobacco mosaic viruses on cationic lipid monolayers. J Colloid Interface Sci. 2011;358:497–505. https://doi.org/10.1016/j.jcis.2011.03.048.
73. Poghossian A, Schöning MJ. Label-free sensing of biomolecules with field-effect devices for clinical applications. Electroanalysis. 2014;26:1197–213. https://doi.org/10.1002/elan.201400073.
74. Kaisti M. Detection principles of biological and chemical FET sensors. Biosens Bioelectron. 2017;98:437–48. https://doi.org/10.1016/j.bios.2017.07.010.
75. Koch C, Wabbel K, Eber FJ, Krolla-Sidenstein P, Azucena C, Gliemann H, et al. Modified TMV particles as beneficial scaffolds to present sensor enzymes. Front Plant Sci. 2015;6:1137. https://doi.org/10.3389/fpls.2015.01137.
76. Prasad B, Lal R. A capacitive immunosensor measurement system with a lock-in amplifier and potentiostatic control by software. Meas Sci Technol. 1999;10:1097–104. https://doi.org/10.1088/0957-0233/10/11/321.
77. Shrivastava A, Gupta V. Methods for the determination of limit of detection and limit of quantitation of the analytical methods. Chron Young Sci. 2011;2:21–5. https://doi.org/10.4103/2229-5186.79345.
78. Manocchi AK, Horelik NE, Lee B, Yi H. Simple, readily controllable palladium nanoparticle formation on surface-assembled viral nanotemplates. Langmuir. 2010;26:3670–7. https://doi.org/10.1021/la9031514.

Melanie Welden is a postdoctoral researcher at the Institute of Nano- and Biotechnologies (INB) at FH Aachen University of Applied Sciences. Her research focuses on the development of biocompatible and bioresorbable biosensors, as well as the use of tobacco mosaic virus particles as nanocarriers for the immobilization of biomolecules on biosensors.

Arshak Poghossian is head of the company MicroNanoBio and Foreign Member of the Armenian National Academy of Sciences. His research interests are semiconductor chemical sensors and biosensors, biosensing modelling, surface and interfacial phenomena, sensor materials, nano-devices, and nano- and biotechnology.

Christina Wege is head of the Research Unit Molecular and Synthetic Plant Virology at the University of Stuttgart, Institute of Biomaterials and Biomolecular Systems, Germany. Her research focuses on the redesign and functionalization of plant viral building blocks in "green" nanomaterials for technical and biomedical uses, and on the molecular biology of important plant virus diseases.

Michael J. Schöning is founding director of the Institute of Nano- and Biotechnologies (INB), Jülich, Germany, at FH Aachen University of Applied Sciences. His main research subjects concern silicon-based chemical sensors and biosensors, thin-film and thick-film technologies, solid-state physics, and micro- and nano(bio-)system technology.